Master's Thesis

Nanobead-reinforced outmost shell of solid-electrolyte interphase layers for suppressing dendritic growth of lithium metal

Minsoo Kim

Department of Energy Engineering

Graduate School of UNIST

2018

Nanobead-reinforced outmost shell of solid-electrolyte interphase layers for suppressing dendritic growth of lithium metal

Minsoo Kim

Department of Energy Engineering

Graduate School of UNIST

Nanobead-reinforced outmost shell of solid-electrolyte interphase layers for suppressing dendritic growth of lithium metal

A thesis
submitted to the Graduate School of UNIST
in partial fulfillment of the
requirements for the degree of
Master of Science

Minsoo Kim

06 / 14 / 2018 of submission

Approved by

Advisor
Hyun-Kon Song

Nanobead-reinforced outmost shell of solid-electrolyte interphase layers for suppressing dendritic growth of lithium metal

Minsoo Kim

This certifies that the thesis of Minsoo Kim is approved.

06 / 14 / 2018 of submission

signature

Advisor: Hyun-Kon Song

signature

Sang-Young Lee: Thesis Committee Member #1

signature

Nam-Soon Choi: Thesis Committee Member #2

Abstract

Plating-stripping reversibility of lithium metal was improved by reinforcing the solid-electrolyte interphase (SEI) layer by inorganic nanobeads during formation of the SEI layer. The outmost SEI shell (OSS) was clearly identified, which is the SEI layer formed on current collectors (or lithium metal) before the first lithium metal deposition. The OSS was intrinsically brittle and fragile so that the OSS was easily broken by lithium metal dendrites growing along the progress of plating. Lithium metal deposit was not completely stripped back to lithium ions. On the other hand, lithium metal cells containing inorganic nanobeads in electrolyte showed high reversibility between plating and stripping. The nanobeads were incorporated into the OSS during the OSS formation. The nanobead-reinforced OSS having mechanically durable toughness suppressed dendritic growth of lithium metal, not allowing the dendrites to penetrate the OSS. In addition to the mechanical effect of nanobeads, the LiF-rich SEI layer formation was triggered by HF generated by the reaction of the moisture adsorbed on oxide nanobeads with PF_6^-. The LiF-rich composition was responsible for facile lithium ion transfer through the SEI layer and the OSS in the presence of nanobeads.

Contents

List of figures

at room temperature for the different ratios of salt-to-solvent.

Figure 7. Electrochemical performance of lithium-sulfur batteries. (a) Voltage profiles of the first cycle of C/S electrodes in electrolytes with different ratios of LiTFSI to DOL:DME (1:1 by volume). **(b)** Cycle performance of cells in electrolytes with different ratios of LiTFSI to DOL:DME (1:1 by volume). **(c)** Coulombic efficiency at a current density of 0.2 C. **(d)** Rate performance of cells in electrolytes with different ratios of LiTFSI to DOL:DME (1:1 by volume).

Figure 8. Tools for patterning lithium metal and morphologies of patterned Li metal. (a) A digital image of the stamp for pattering. SEM images of patterned Li metal at **(b)** the top view and **(c)** the cross-sectional view and images at **(d-f)** the different magnification.

Figure 9. Electrochemical properties of lithium symmetrical cells using patterned lithium metal. (a) Potential profiles of Li/Li symmetrical cells using bare Li metal and patterned Li metal (0.53 mA cm^{-2} (30 min) → Rest (10 min) → − 0.53 mA cm^{-2} (30 min) → Rest (10 min)). **(b)** Nyquist plots of the Li/Li symmetrical cells after cycling. **(c)** Rate performance of cells using bare Li metal and patterned Li metal. **(d)** Coulombic efficiency of using bare Li metal and patterned Li metal.

Figure 10. Lithium metal plating/stripping reversibility. Electrolyte = 1M $LiPF_6$ in EC/DEC at 1:1 v/v with 5 wt. % FEC. (**a**) Coulombic efficiency (C. E.) of Li || Cu cells. Lithium metal was Galvano-statically plated at 1 mA cm^{-2} up to 1 mAh cm^{-2} and stripped at the same rate. (**b**) Potential (*E*) profiles along cycle for (**a**). (**c**) Oxide content dependency of cycle life. The cycle life was defined as the cycle number at which the coulombic efficiency falls below 80 %. Averages and standard deviations were calculated from three different independent tests. (**d**) Potential profiles at the 10^{th} and 50^{th} cycles, taken from (b).

Figure 11. Identifying the OSS. Lithium metal was repeatedly plated and stripped on copper current collectors at the same condition of **Figure 10**. The lithium salt was changed to $LiClO_4$ instead of $LiPF_6$. Cross-sections of the copper current collectors on which lithium metal was plated after 20 plating/stripping cycles were investigated by scanning electron microscopy (SEM) and energy dispersive X-ray spectroscopy (EDS). (**a** to **c**) SEM images (top) and EDS profiles of elements (middle for F and bottom for Si or Al) along cross-sections of electrodes. Lithium metal was plated and stripped in the presence of: (**a**) no nanobeads, (**b**) 0.9 vol. % silica and **(c)** 0.9 vol. % alumina. The right-side faces are the electrode surfaces exposed to electrolyte in cells. 10 μm scale bars were indicated.

Figure 12. Morphology of lithium metal deposits plated on copper substrates. The electrolyte and the cycling condition were the same as those of **Figure 10**. (**a** to **i**) SEM images of the electrodes in the presence of: (**a** to **c**) no nanobeads, (**d** to **f**) 0.9 vol. % silica and (**g** to **i**) 0.9 vol. % alumina. The left images are for the cross-sectional views of lithium metal deposits obtained after the first plating. The middle and right images are for the cross-sectional and top views of lithium metal deposits obtained after the 20^{th} plating following 19 plating/stripping cycles. 10 μm scale bars were indicated while the scale bar in the inset is 1 μm.

Figure 13. LiF ratio in the SEI layers of each lithium deposit with and without oxide nanobeads. Ratio was calculated from the peak area of each $Li_xP_yOF_z$ and LiF in XPS data of **figure 14**.

Figure 14. Chemical compositions of OSS. The cycling condition was the same as that of **Figure 10**. 1 wt. % nanobeads were used, which were equivalent to 0.5 vol. % silica and 0.3 vol. % alumina. The $LiPF_6$-based electrolyte of **Figure 10** was used for XPS measurement (**a** and **b**) while the lithium salt was changed to $LiClO_4$ at the same concentration for **c**. (**a**) F 1s XPS spectra. (**b**) The change of the atomic ratio occupied by F with etching time. The F atomic ratio was calculated in consideration of the peak area and relative intensity factor. (**c**) The coulombic efficiency of Li||Cu cells along cycles in the presence of 1 M $LiClO_4$. (**d**) Contribution analysis of mechanical and chemical factors. The effects of the factors were quantified by comparing the cycle life (Cyc80) between the absence and the presence of nanobead in $LiClO_4$ and between the absence and the presence of PF_6^- with nanobeads. Cyc80 was defined as the cycle number at which the coulombic efficiency falls below 80 %.

Figure 15. Charge transfer resistances (R_{ct}) of Li^+/Li^0 electrochemistry on 3 hours and 3 days after cell assembly. (**a** and **b**) Impedance spectra of Li||Li cells. Potential was biased at the open circuit potential around 0 V_{Li}. The $LiPF_6$-based electrolyte of **Figure 10** was used. (**c** and **d**) Nanobead content dependency of R_{ct}. Averages and standard deviations were calculated from three different independent tests. Impedances were measured on 3 hours (**a** and **c**) and 3 days (**b** and **d**) after the cell assembly.

List of tables

List of schemes

Nomenclature

LIBs	**Lithium ion batteries**
LCO	Lithium cobalt oxide, $LiCoO_2$
LMO	Lithium manganese oxide, $LiMn_2O_4$
LFP	Lithium iron phosphate ($LiFePO_4$
EV	Electric vehicles
ESS	Energy storage system
IoT	Internet of things
Mn	Manganese
Ni	Nickel
Li	Lithium
SEI	Solid-electrolyte interphase
FEC	Fluoroethylene carbonate
PDMS	Poly(dimethylsiloxane)
PAN	Polyacrylonitrile
Nafion	Sulfonated tetrafluoroethylene copolymer
OSS	Outmost SEI shell
EC	Ethylene carbonate
DEC	Diethyl carbonate
SEM	Scanning electron microscope
EDS	Energy dispersive X-ray spectroscope
XPS	X-ray photoelectron spectroscope
R_{ct}	Impedance of charge transfer
TMOS	Tetramethylorthosilicate
DOL	Dioxolane
DME	Dimehtyl ether
LiTFSI	Lithium bis(trifluoromethanesulfonyl)imide

I. Introduction

1.1. What is lithium ion batteries?

Lithium ion batteries (LIBs) are named due to the role of lithium ions as charge carriers when they are charged or discharged. Lithium ion batteries consist of 4 major components: cathodes, anodes, separators and electrolytes. Cathodes such as lithium cobalt oxide ($LiCoO_2$, LCO), lithium manganese oxide ($LiMn_2O_4$, LMO) and lithium iron phosphate ($LiFePO_4$, LFP) are the sources of lithium ions existing in the lattice structure of transition metals and oxides.[1] Anodes such as graphite and silicon are capable of taking and releasing lithium ions from and to cathodes as intercalation and alloying reaction. Electrolytes act the media between two electrodes: cathodes and anodes.[2] Li ions existing in electrolytes move from anodes to cathode during discharging and move reversely during charging while electrons move in external circuit.

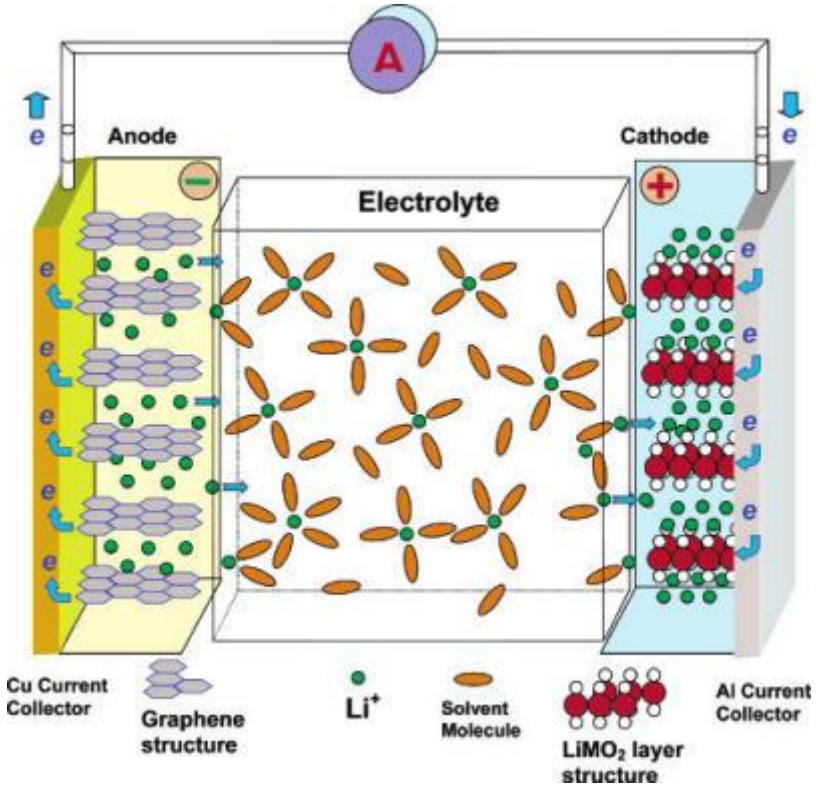

Scheme 1. Working mechanism of lithium ion batteries. Main components are cathode, anode, electrolyte and separator.[2]

1.2. The demand and direction of development of lithium ion batteries

The demand for electric vehicles (EV) has grown as the effort to reduce air pollution from fossil fuel. And the market of energy storage system (ESS) has also increased due to the demand for alternative energy such as wind power, sunlight generation. Therefore, LIBs have become one of the most important technologies in the society as LIBs are the critical technology in EV and ESS. Indeed, our industry is advancing forward forth industrial revolution represented by internet of things (IoT).[3] And IoT means that each object is networked and share information with each other and individual power supplies are necessary.

a

Modes of operation	battery capacity needed, kWh	Energy density, Wh/kg	Weight of battery, Kg	Speed, kilometres per hour	Distance on one charge, kilometres
 Hybrid	<3	40-50 (Ni-MH)	60 (Ni-MH)	100+	15
 Plug in Hybrid	5.6-18	90-100 (Li-ion)	60-200 (Li-ion)	100+	10-60
 Full EV	35-54	90-100 (Li-ion)	450 (Li-ion)	>100	150-200

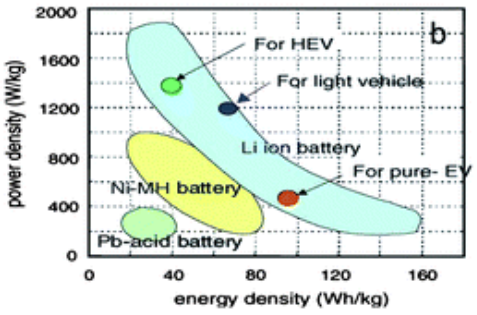

Figure 1. (a) Properties for three types of electric vehicles (EV): hybrid EV (HEV), plugged hybrid EV (PHEV) and full EV. **(b)** Ragone plot for batteries showing that power density and energy density of each battery and EVs.[4]

As the demand, researchers are trying to develop better batteries with higher capacity, better capacity retention, higher charging rate and better safety. In the case of cathode, LCO has the limitation of practical capacity due to its severe structure change causing irreversibility. Therefore, other transition metals such as manganese (Mn) and nickel (Ni) are used for alternatives of LCO.[5] Furthermore, Ni-rich[6] or over-lithiated oxide (OLO)[7] are under development for much higher capacity. In the case of

anode, carbon-typed materials are mostly used. These carbon materials are sorted out as graphitic and non-graphitic carbon. Graphitic carbon has the theoretical capacity of 372 mAh g^{-1} and almost approached the limitation of theoretical practically.[8] Hence, researchers have tried to develop other materials for anodes. Silicon is one of the candidates for anodes of LIBs, which has the theoretical capacity of about 4200 mAh g^{-1}.[9] However, silicon has the severe problem of volume expansion during lithiation. Therefore, develops are trying to use small amount of silicon with carbon materials to reduce volume expansion.

1.3. Lithium metal as anode materials

Recently, lithium metal has been reconsidered as anode materials due to its characteristics: high capacity of 3860 mAh g^{-1} and the most negative reduction potential at -3.040 V versus standard hydrogen electrode.[10] Plating/stripping of lithium metal could replace intercalation/de-intercalation of lithium ions to/from host materials in presently available lithium ion batteries (LIBs). Next generation energy storage devices such as Li-S and Li-air batteries have been developed with lithium metal as anodes because lithium metal could be lithium source itself instead of cathodes.

However, dendritic growth of lithium metal along repeated plating/stripping causes critical problems including (1) short-circuit between anodes and cathodes and (2) low coulombic efficiency. First, needle-like dendrites, which have much larger yield strength than bulk lithium metal, penetrate separators and reach cathodes. [11] High currents flowing along the dendrites shorting cells result in thermal runaway of cells.[12-13] Second, the fresh conductive surface generated by lithium metal plating triggers cathodic decomposition of electrolyte molecules to form solid-electrolyte interphase (SEI) layers. The side reactions are irreversible so that the electrons consumed for SEI formation are not recovered during lithium metal stripping. Charges are lost even during stripping process. A portion of lithium metal loses its contact with electric pathways when the bottom parts of dendrites are stripped before the tip parts are stripped completely.[14]

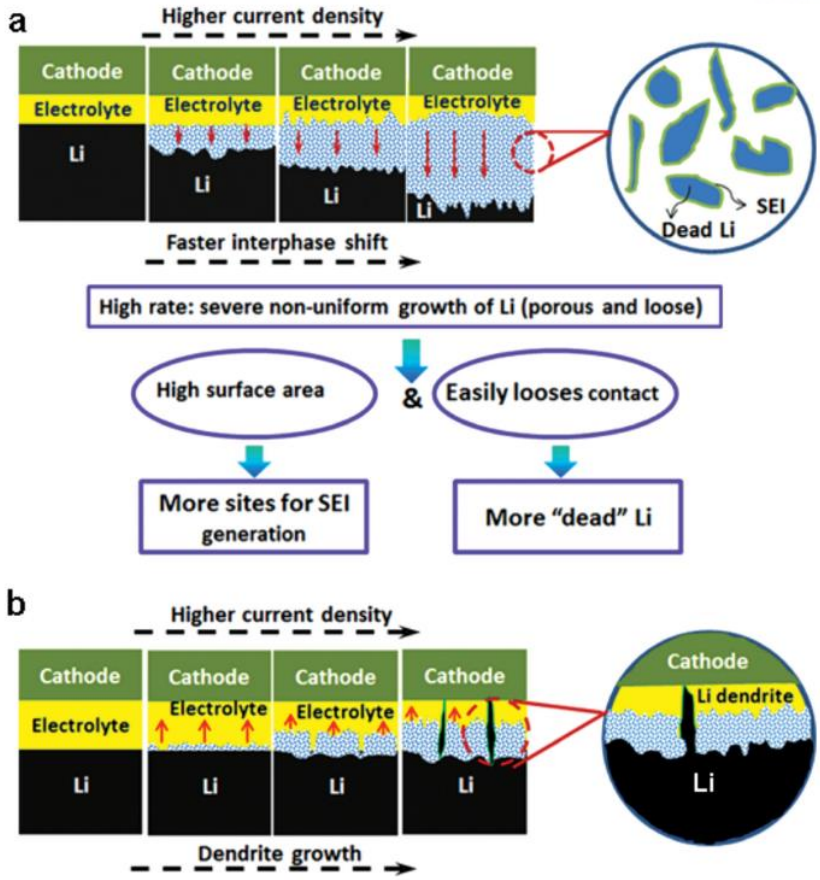

Scheme 2. Failure mechanism by lithium dendrites. (a) Formation and stacks of dead lithium, increasing overpotential. **(b)** Growth of lithium dendrites and short circuit by lithium dendrites connecting cathode to anode. [13]

Due to the flaws of lithium metal, the insertion/de-insertion electrochemistry of lithium *ions* has been preferred to the deposition/stripping electrochemistry of lithium *metal*.[1, 15] Recently, the use of lithium metal as anodes was revisited to achieve high energy densities. The key technology centered on lithium *metal* batteries is to suppress dendritic growth of lithium metal during deposition. Ideally, lithium-free copper electrodes are enough if the lithium provided by cathode materials is deposited without loss during charge and then stripped in a completely reversible manner during discharge.

1.4. Strategies to suppress dendritic growth of lithium metal

Suppressing dendritic growth of lithium metal is most important for applying lithium metal as anodes. The approaches for suppressing dendrites are classified mainly three parts: (1) protective layers, (2) modification of bulk electrolyte and (3) modification of electrode. Many researchers tried to suppress dendrites mechanically by using artificial protective layers. Peng et al.[16] coated the surface of lithium metal with alumina particles with the help of polymer binders. Porous layers with alumina have good chemical stability and suppress lithium dendrites mechanically. As a result, the coulombic efficiency of Li||Cu cells with porous layers and fluoroethylene carbonate (FEC) additives achieved 97.6 % for over 50 cycles, while cells with only FEC additives dropped to 35 % in the 50th cycle.

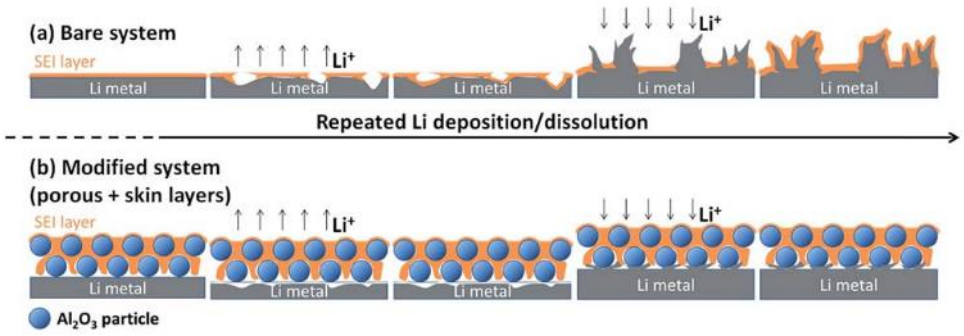

Scheme 3. The morphology of lithium metal deposition **(a)** with only SEI layers on the surface of lithium metal and **(b)** with volumetric confining surface layer containing alumina particles and polymer binders (porous + skin layers).[16]

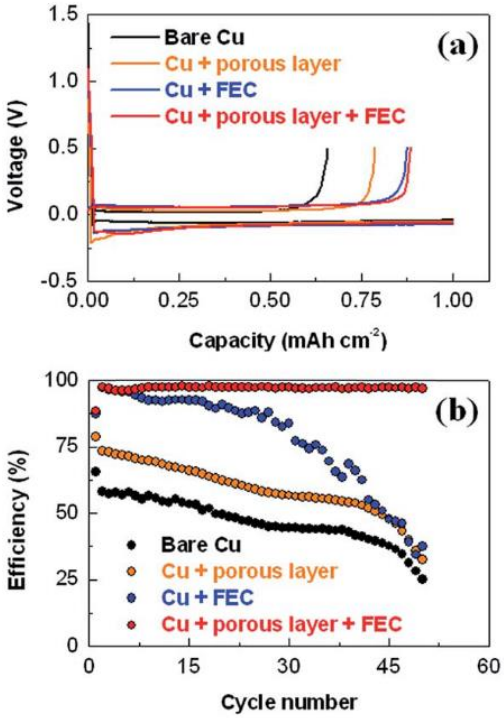

Figure 2. Cycling performance of Li||Cu cells. (a) Voltage profiles of the 1st cycle of bare Cu, Cu with porous layer, Cu with FEC and Cu with porous layer + FEC. **(b)** Coulombic efficiencies at the condition of 0.5 mA cm^{-2}. The amount of lithium plated in each cycle is 1 mAh cm^{-2}. [16]

Zhu et al.[17] modified the surface of lithium metal with poly(dimethylsiloxane) (PDMS) film with nanopores. They said that nanopores in the PDMS film let lithium ions pass through the film and PDMS film has good chemical and electrochemical stability so that lithium dendrites could be suppressed. Modified lithium metals maintained 90 % of coulombic efficiency for more than 100 cycles, while the coulombic efficiency of lithium metals without PDMS film dropped to 20 % in 30 cycles at the condition of 1 mAh cm^{-2}.

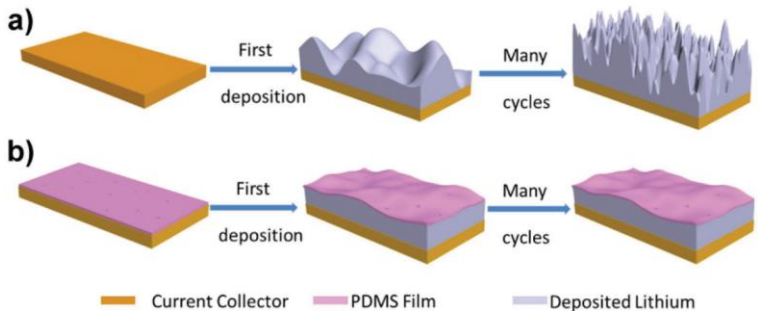

Scheme 4. Schematic figures of lithium depositions. (a) The morphology of lithium deposition on Cu substrates at the first cycle and after many cycles. **(b)** The morphology of lithium deposition on Cu substrates with PDMS film at the first cycle and after many cycles. [17]

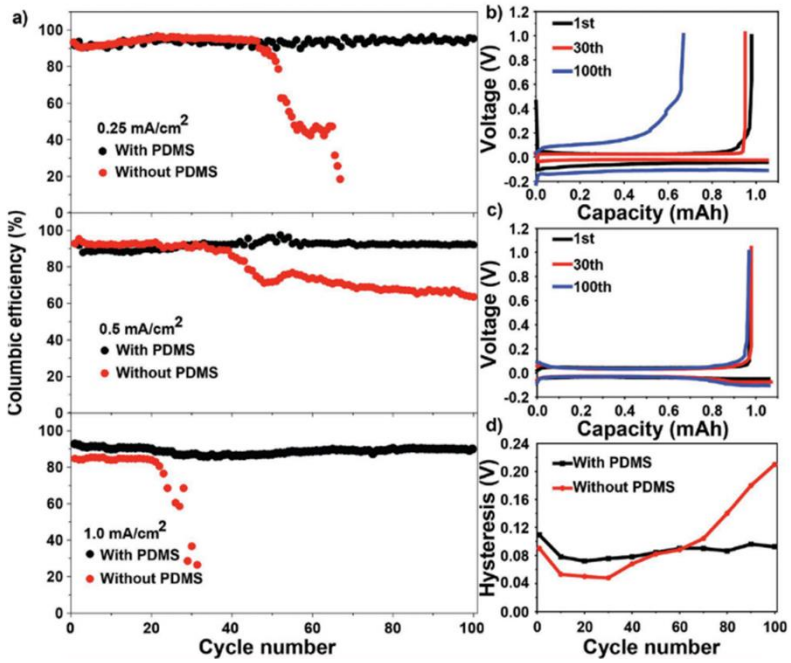

Figure 3. Cycle performance of bare Cu foil and modified Cu foil with PDMS film. (a) The coulombic efficiency of bare Cu and modified Cu with PDMS film at difference densities with the lithium deposition of 1 mAh cm^{-2}. **(b)** Voltage profiles of Cu foil electrode at different cycles at the current density of 0.5 mA cm^{-2}. **(c)** Voltage profiles of Cu foil electrode with PDMS film at different cycles at the current density of 0.5 mA cm^{-2}. **(d)** Voltage hysteresis between lithium plating and stripping for the electrodes with and without PDMS at the current density of 0.5 mA cm^{-2}.[17]

Lang et al.[18] arranged polyacrylonitrile (PAN) submicron fibers on copper substrates with the form of grid so that polymer fiber array could allow the uniform dispersion and deposition of lithium ions. They achieved good cycle retention of lithium metal anode with the coulombic efficiency of 97.4 % during 250 cycles under the condition of 1 mA cm-2 and 1 mAh cm-2.

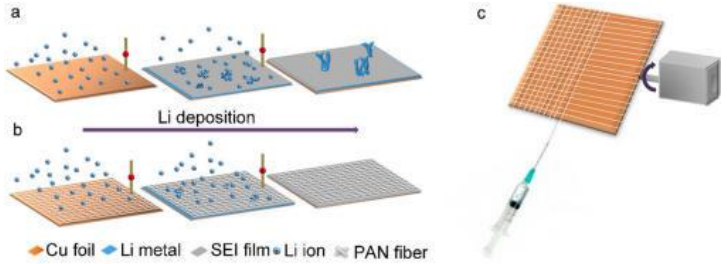

Scheme 5. Schematic figure of lithium deposition and methods for fabricating PAN-Cu electrode. (a) Lithium deposition on bare Cu foil. **(b)** lithium deposition on PAN-Cu electrode. **(c)** The method for fabricating PAN-Cu electrode.[18]

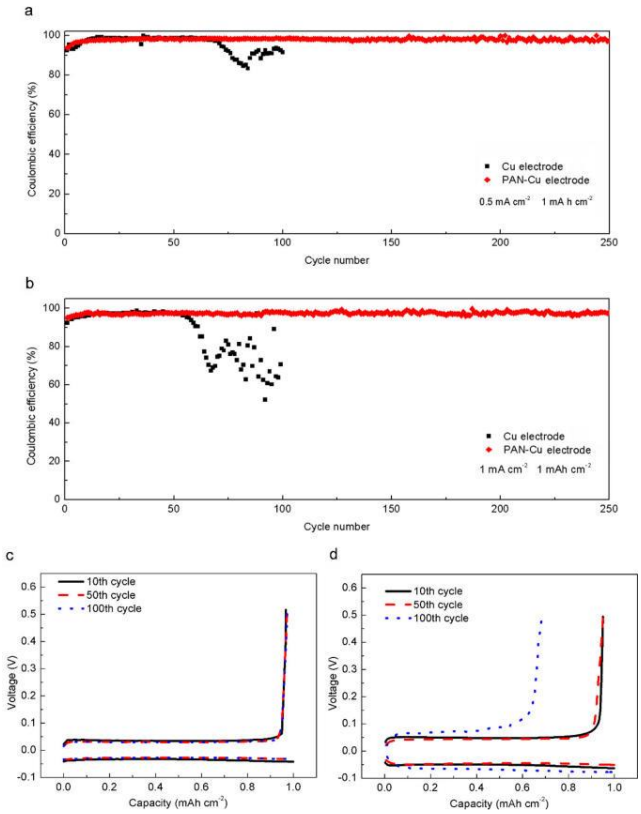

Figure 4. Cycle performances of Cu electrode and PAN-Cu electrode. (a) The coulombic efficiency of lithium plating/stripping on bare Cu and PAN-Cu at the current density of 1 mA cm^{-2} and Li deposition of 1 mAh cm^{-2}. **(b)** The coulombic efficiency of lithium plating/stripping on bare Cu and PAN-Cu at the current density of 0.5 mA cm^{-2} and Li deposition of 1 mAh cm^{-2}. **(c)** The voltage profiles of lithium platin/stripping on bare Cu at the current density of 1 mA cm^{-2} and Li deposition of 1 mAh cm^{-2}. **(d)** The voltage profiles of lithium platin/stripping on PAN-Cu at the current density of 1 mA cm^{-2} and Li deposition of 1 mAh cm^{-2}.[18]

The direction of modifying electrolyte is mainly enhancing Li ion flux such as cation transference number.[19-21] Lu et al.[19] showed ionomer membranes by lithiating a sulfonated tetrafluoroethylene copolymer (Nafion) to allow only lithium ions pass through electrolytes while anions are fixed on the polymer backbone. As a result, transference number of lithium cations increased and the time for causing short circuit by lithium dendrite was delayed according to the Sand's time which is the expected dendrite nucleation time and is proportional to transference number of lithium cations.

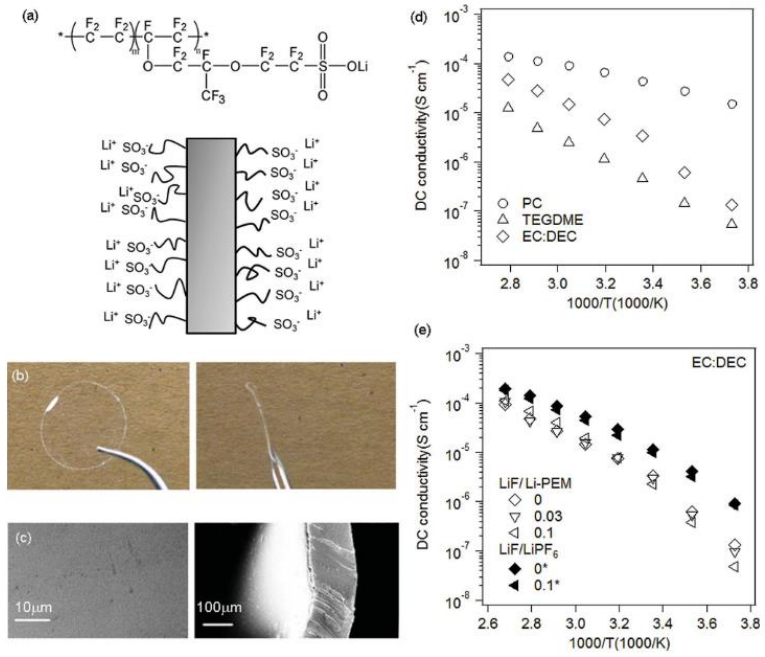

Figure 5. (a) Chemical structure and schematic figure of Li-PEM. **(b)** Digital images of top and cross-section pictures of Li-PEM. **(c)** SEM images of top view and cross-sectional view of Li-PEM. **(d)** DC conductivity as a function of temperature for Li-PEM with different organic solvents. **(e)** DC conductivity as a function of temperature for Li-PEM (hollow) and $LiPF_6$ (solid) in EC:DEC with different molarities of LiF.[19]

Suo et al.[20] demonstrated the effect of 'solvent-in-salt' electrolyte on the lithium metal anodes by adding ultrahigh amount of salts in solvent. They said that the amount of free lithium ions increased and large anion could be dragged in the high viscosity system, which leading to much higher transference number of lithium cations. They showed improved performance of Li-S batteries.

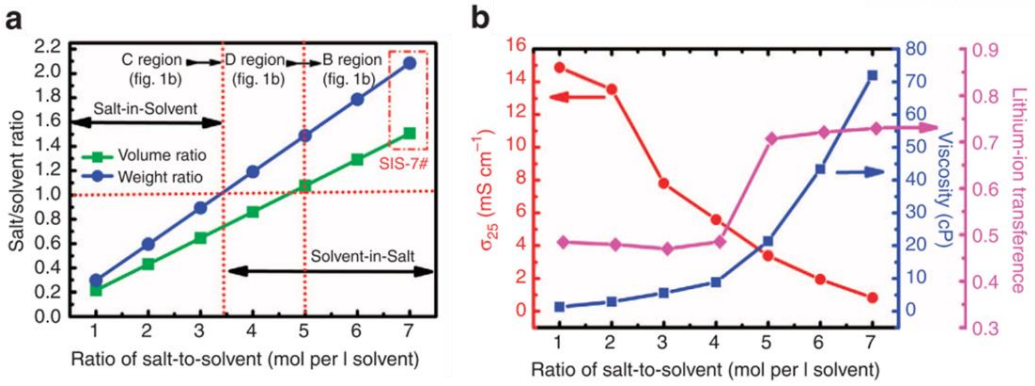

Figure 6. physicochemical properties of 'Solvent-in-Salt' electrolytes. (a) Volumetric and gravimetric ratio of salt/solvent as a function of ratio of salt-to-solvent: LiTFSI salts and solvents of DOL:DME (1:1 by volume). **(b)** Ionic conductivity, viscosity and lithium cation transference number at room temperature for the different ratios of salt-to-solvent.[20]

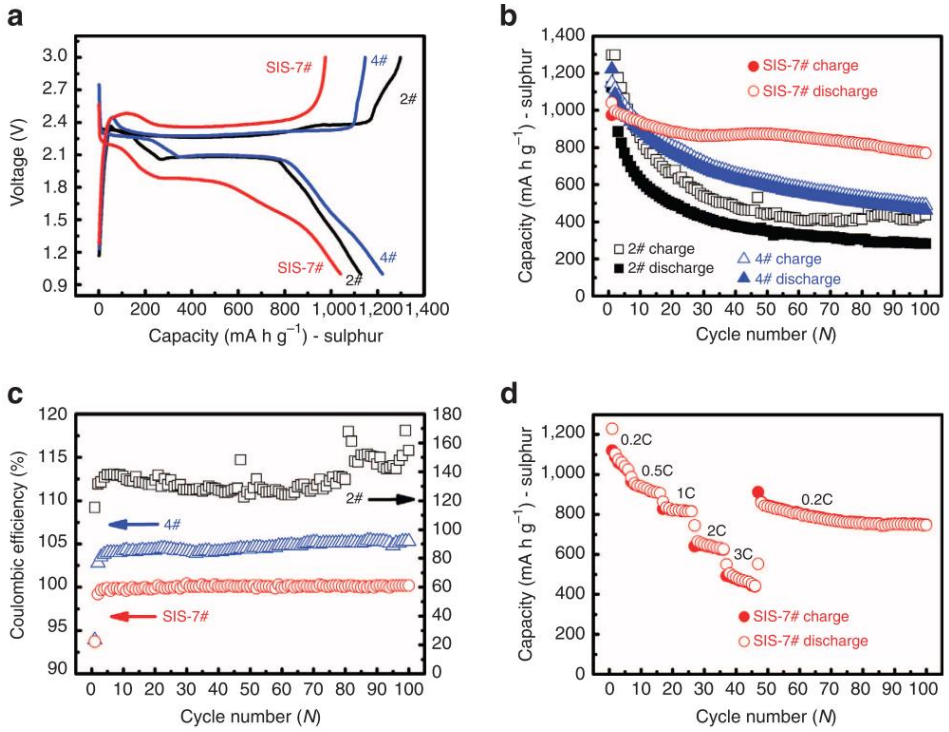

Figure 7. Electrochemical performance of lithium-sulfur batteries. (a) Voltage profiles of the first cycle of C/S electrodes in electrolytes with different ratios of LiTFSI to DOL:DME (1:1 by volume). **(b)** Cycle performance of cells in electrolytes with different ratios of LiTFSI to DOL:DME (1:1 by volume). **(c)** Coulombic efficiency at a current density of 0.2 C. **(d)** Rate performance of cells in electrolytes with different ratios of LiTFSI to DOL:DME (1:1 by volume).[20]

The other effort is distributing current density and lowering the effective current density by enlarging the surface area of electrodes.

Park et al.[22] tried to make micro-patterned holes on the surface of lithium metal so that lithium metals could be deposited and stripped selectively at the holes. They showed current density was concentrated on the tips of the holes on the lithium metal by using COMSOL Multiphysics.

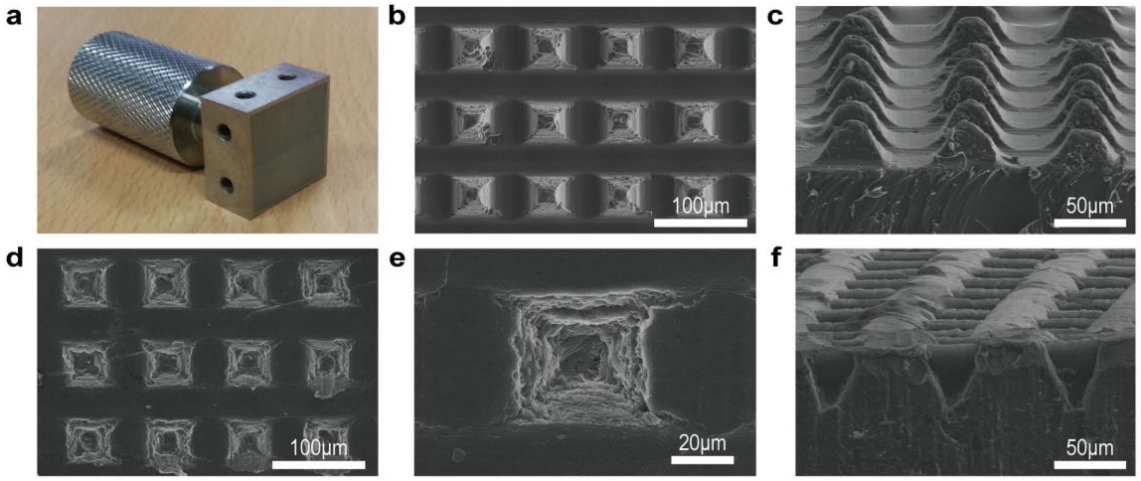

Figure 8. Tools for patterning lithium metal and morphologies of patterned Li metal. (a) A digital image of the stamp for pattering. SEM images of patterned Li metal at **(b)** the top view and **(c)** the cross-sectional view and images at **(d-f)** the different magnification.[22]

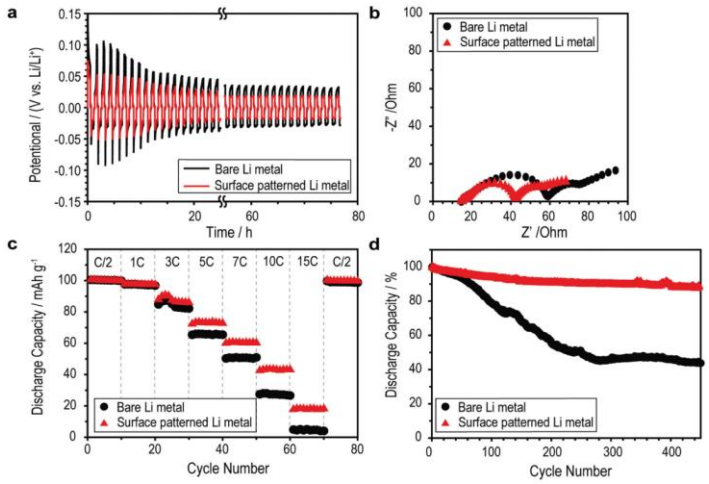

Figure 9. Electrochemical properties of lithium symmetrical cells using patterned lithium metal. (a) Potential profiles of Li/Li symmetrical cells using bare Li metal and patterned Li metal (0.53 mA cm^{-2} (30 min) → Rest (10 min) → − 0.53 mA cm^{-2} (30 min) → Rest (10 min)). **(b)** Nyquist plots of the Li/Li symmetrical cells after cycling. **(c)** Rate performance of cells using bare Li metal and patterned Li metal. **(d)** Coulombic efficiency of using bare Li metal and patterned Li metal.[22]

Zhang et al.[23] made conductive nanostructured scaffolds of graphene flake to distribute local current

density. The Sand's time, which is correlated with short circuit time, is inverse proportional to the effective electrode current density. And scaffold structure lead to lower effective current density, letting less dendritic growth of lithium metal formed.

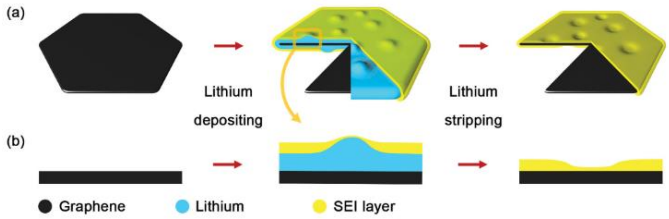

Scheme 6. Schematic figure of lithium plating and stripping on graphene flake. The scheme before lithium deposition, after deposition and after stripping of **(a)** a graphene flake and **(b)** the cross-sectional view. Lithium (blue) is deposited and stripped under the protection of SEI layers (yellow) on the surface of graphene flake (black).[23]

1.5. The role of SEI layers on suppressing lithium dendrites

Electrolyte molecules are decomposed to form SEI layers on lithium metal anode due to the negative reduction potential of Li^+/Li^0; or on copper current collector when negative potentials below 1 V versus Li/Li^+ (V_{Li}) is applied. This initial SEI layer conformably formed along anode surface is defined as the *outmost SEI shell* (OSS) in this work (OSS in **Scheme 7a**). The electrically-insulating nature of the SEI layer prevents electrolytes from being reduced while the ionically-conductive nature of the SEI layer allows lithium ions to pass. Additional lithium is deposited between the OSS and the anodes (or current collectors) during charge. The OSS generated by widely used electrolyte molecules such as carbonates and $LiPF_6$ are not mechanically strong enough to endure penetration of growing lithium metal dendrites. The continuous integrity of the OSS is lost as deposition/stripping is repeated (**Scheme 7a**).

Durable toughness of OSS was improved for dendritic growth suppression by using SEI-forming additives like fluoroethylene carbonate (FEC).[24-26] Robust OSS generated by FEC increased coulombic efficiency from 88 % to 96 % at the 50th cycle (**Scheme 7b**).[25] However, the deposition/stripping reversibility achieved by the use of SEI-forming agents was still not satisfactory. As a more aggressive strategy to support OSS toughness, artificial protective layers were laminated on anodes for mechanically suppressing dendritic growth [16, 27-29]. As a representative example, alumina powder was coated on lithium metal by the help of a polymer binder.[16] The polymer/oxide composite lamina supports weak OSS against protruding metal dendrites. The cycles showing higher than 95 % efficiency lasted during 50 cycles in the modified cells while the bare cells showed 35 % efficiency at 50 cycles.[19-21]

In this work, we reinforced OSS by nanobeads for preventing dendritic penetration. Oxide nanoparticles as nanobeads were simply introduced to practical $LiPF_6$-containing carbonate electrolytes of LIBs. Different from previously reported artificial protective layers *pre-coated* on anodes, inorganic nanobeads were incorporated into OSS *in situ* during the OSS formation. Reversibility of lithium metal deposition/stripping was dramatically improved in the presence of the nanobead-suspended electrolytes. Highly efficient reversibility was prolonged from ~40 cycles to >100 cycles by the help of the *in situ* OSS reinforcement by nanobeads. Integrity of the nanobead-reinforced OSS remained unbroken and well maintained (**Scheme 7c**) while bare OSS is completely disassembled after repeated deposition/stripping cycles (**Scheme 7a**).

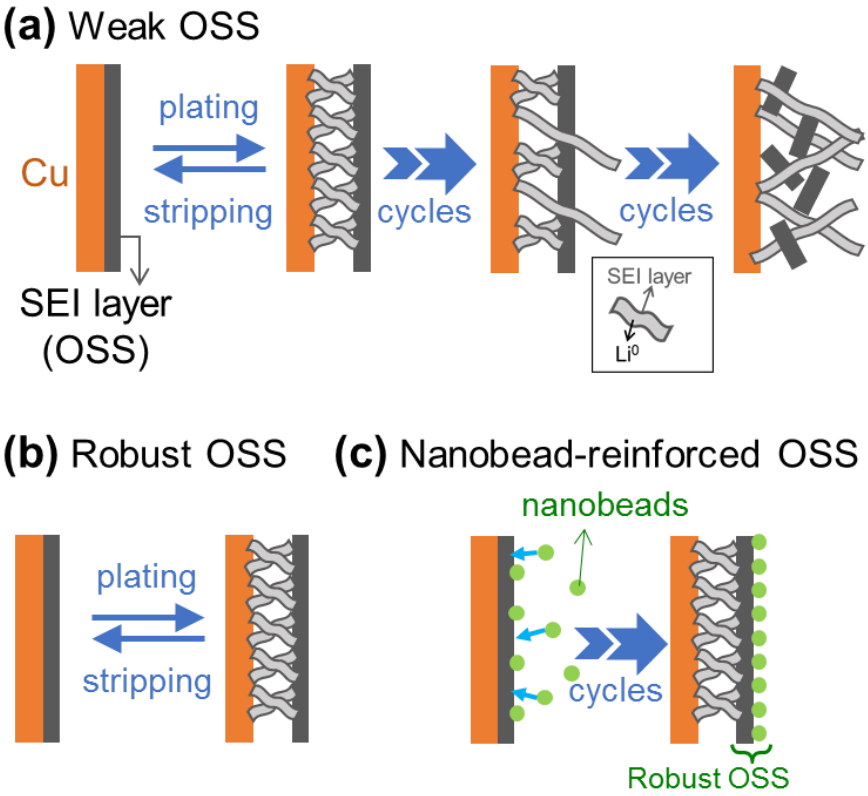

Scheme 7. Outmost SEI layer shell (OSS). (**a**) Weak OSS, which is fragmented by overgrown dendrites after repeated cycles of plating and stripping. (**b**) Robust OSS. Plating and stripping of lithium metal was reversible in the presence of *robust* OSS. (**c**) Nanobead-reinforced OSS guaranteeing plating/stripping reversibility of lithium metal.

II. Experimental Method & Materials

2.1. Cell preparation

The 2032 coin cells were assembled with lithium foil and copper foil as electrodes (Li||Cu) for cyclability tests or with two lithium foils (Li||Li) for impedance measurement in a glove box (MBRAUN) with less than 1 ppm of H_2O. Polyethylene separator (Tonen F16BME) was sandwiched between the electrodes. 1M $LiPF_6$ in a mixture of ethylene carbonate and diethyl carbonate (EC / DEC) at 1:1 volumetric ratio with 5 wt. % FEC (Soulbrain) was used as the base electrolyte. Oxide nanobeads, SiO_2 (~12 nm) or Al_2O_3 (~13 nm) nanoparticles (Sigma Aldrich), were dispersed in the base electrolyte. The amount of nanobeads introduced to electrolytes were controlled in terms of volume percentage (vol. %). The weight percentages (wt. %) were converted to vol. % by using the sizes and densities of nanobeads and electrolyte: density (g cm^{-3}) = 1.26 for 1 M $LiPF_6$ in EC/DEC at 1:1 volumetric ratio, 2.6 for silica and 4 for alumina.

2.2. Electrochemical characterization

The Li||Cu cells were pre-cycled prior to the cyclability tests. First, they were cycled 5 times from 0 V_{Li} to 1.5 V_{Li} at 25 μA cm^{-2} to form the stable SEI layer. Second, lithium metal was plated on copper at 0.1 mA cm^{-2} up to 1 mAh cm^{-2} and stripped from copper at the same current density up to 1 V. This second slow plating/stripping cycle was repeated 2 times to plate non-dendritic lithium deposit. Then the same amount of lithium metal (1 mAh cm^{-2}) was plated and stripped at 1 mA cm^{-2} repeatedly for obtaining cyclability information. Impedance spectra were obtained for Li||Li symmetric cells to obtain the information on lithium ion transport through the SEI layer. The impedance was measured from 100 mHz to 1 MHz at the open circuit potential around 0 V versus Li^+/Li (V_{Li}) (BioLogic, SP 300).

2.3. Physicochemical Characterization

Lithium deposits on copper electrodes were characterized microscopically and spectroscopically by a scanning electron microscope (SEM, Hitach FE-SEM S-4800) equipped with energy dispersive X-ray spectroscope (EDS) and an X-ray photoelectron spectroscope (XPS, Thermo Fisher ESCALAB 250XI).

	Zeta potential	Specific surface area	Ionic conductivity	Density
SiO_2	-13.5 mV	175-225 $m^2 g^{-1}$	8.47 mS cm^{-1}	2.6 g cm^{-3}
Al_2O_3	+44.1 mV	85-115 $m^2 g^{-1}$	8.85 mS cm^{-1}	4.0 g cm^{-3}

*Ref: 8.57 mS cm^{-1}

Table 1. Characteristics of silica and alumina nanoparticles.

III.Results and discussion

3.1. Plating/stripping reversibility

The expected effects of the OSS reinforcement by nanobeads on the reversibility of lithium metal plating and stripping were confirmed. Lithium metal was plated and stripped repeatedly on copper current collectors in Li||Cu cells in a practical $LiPF_6$-based carbonate electrolyte. Two different nanobeads were used: silica or alumina nanobeads were suspended in the carbonate electrolyte. The cells containing oxide nanobeads showed significantly longer cycle life than the cell without nanobeads (**Figure 10a**). Also, the cyclability improvement by nanobeads was clearly shown in potential profiles (**Figure 10b**). When the cycle life is defined as the number of cycle at which the cell's coulombic efficiency reached 80 %, the cycle life of the nanobead-absent control cell was only 40 cycles. The cycle life increased proportionally with the amount of nanobeads up to 140 cycles for 2.2 vol. % silica and ~100 cycles for 2.2 vol. % alumina (**Figure 10c**). The cycle life improvement by silica was superior to that by alumina.

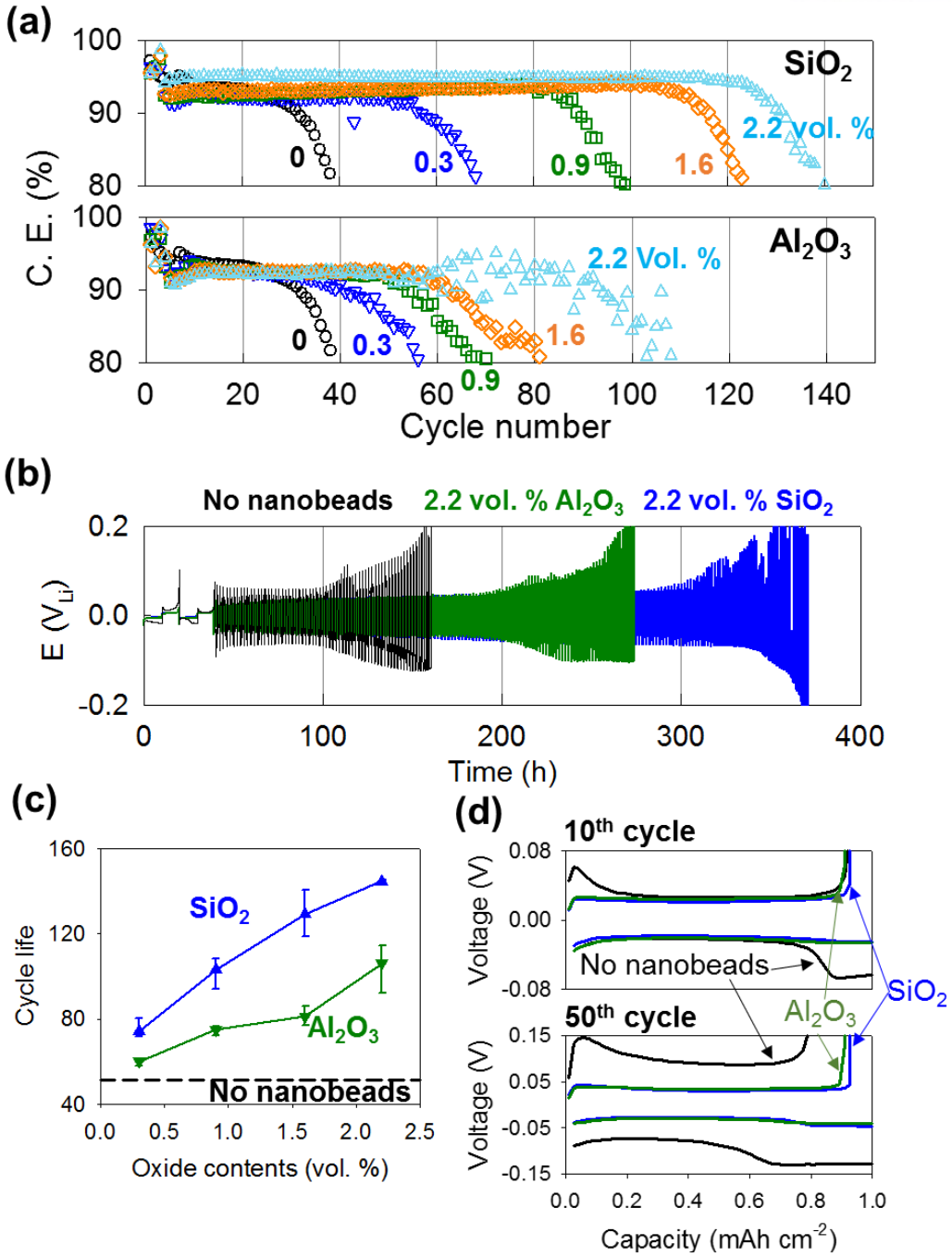

Figure 10. Lithium metal plating/stripping reversibility. Electrolyte = 1M $LiPF_6$ in EC/DEC at 1:1 v/v with 5 wt. % FEC. (**a**) Coulombic efficiency (C. E.) of Li||Cu cells. Lithium metal was Galvano-statically plated at 1 mA cm^{-2} up to 1 mAh cm^{-2} and stripped at the same rate. (**b**) Potential (*E*) profiles along cycle for (**a**). (**c**) Oxide content dependency of cycle life. The cycle life was defined as the cycle number at which the coulombic efficiency falls below 80 %. Averages and standard deviations were calculated from three different independent tests. (**d**) Potential profiles at the 10^{th} and 50^{th} cycles, taken from (b).

Cell voltage profiles of the Li || Cu cells along cycles were closely investigated (**Figure 10d**). At the 10th cycle in the absence of nanobeads, there were overpotentials developed in the latter part of plating processes (-68 mV_{Li} at 0.9 mAh cm^{-2}; V_{Li} = V versus Li/Li^{+}) and the initial part of the following stripping (55 mV_{Li} at 0.05 mAh cm^{-2}). This characteristic overpotential loss was the biggest difference distinguished from the voltage profiles of nanobead-containing cells. Nanobeads suppressed the overpotential potentially developed after lithium metal plating above a critical mass: -24 mV_{Li} at 0.9 mAh cm^{-2} for plating and 23 mV_{Li} at 0.05 mAh cm^{-2} for stripping in the 2.2 vol. % silica-present cell. The potential profiles of the alumina-present cell were almost identical to those of the silica-present cells. As cycles proceeded to the 50th cycle, the difference between the absence and presence of nanobeads was more emphasized. The overpotentials of the nanobead-absent cell were higher than those of the nanobead-containing cells over an entire plating and stripping processes: -104 mV_{Li} (no nanobead) versus -46 mV_{Li} (nanobead) at 0.9 mAh cm^{-2} for plating and 106 mV_{Li} (no nanobead) versus 40 mV_{Li} (nanobead) at 0.05 mAh cm^{-2} for stripping. The nanobead-reinforced OSS, which prevents the penetration of lithium metal dendrites, was responsible for the increase in cycle life.

3.2. Mechanical reinforcement to prevent dendrites from penetrating OSS

Incorporation of inorganic nanobeads into the OSS on Li-plated copper substrates experiencing 20 lithium metal plating/stripping cycles was confirmed by energy dispersive X-ray spectroscopy (EDS) (**Figure 11**). Silicon element was found locally on the surface of lithium metal deposited on copper current collector (bottom of **Figure 11b**) while aluminum element was spread through the lithium metal deposit (bottom of **Figure 11c**).

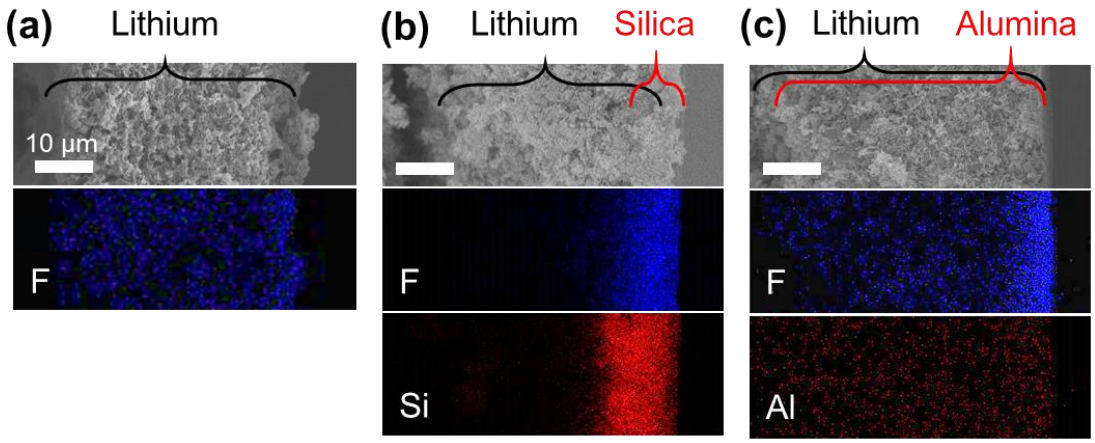

Figure 11. Identifying the OSS. Lithium metal was repeatedly plated and stripped on copper current collectors at the same condition of **Figure 10**. The lithium salt was changed to $LiClO_4$ instead of $LiPF_6$. Cross-sections of the copper current collectors on which lithium metal was plated after 20 plating/stripping cycles were investigated by scanning electron microscopy (SEM) and energy dispersive X-ray spectroscopy (EDS). (**a** to **c**) SEM images (top) and EDS profiles of elements (middle for F and bottom for Si or Al) along cross-sections of electrodes. Lithium metal was plated and stripped in the presence of: (**a**) no nanobeads, (**b**) 0.9 vol. % silica and **(c)** 0.9 vol. % alumina. The right-side faces are the electrode surfaces exposed to electrolyte in cells. 10 μm scale bars were indicated.

A specific experimental condition was required to identify the OSS by fluorine element (F). FEC was used as a SEI-layer-forming agent at a small amount (5 wt. %) that was expected to be completely consumed for the SEI formation before the first metal plating. $LiClO_4$ was used as a non-fluorine lithium salt instead of popularly used $LiPF_6$ to remove F sources except of FEC. The OSS was clearly identified in the surface layer where silica nanobeads were found (middle of **Figure 11b**). F was not found at all in the body of plated lithium metal in the presence of the silica-nanobead-reinforced OSS. The clear F layer confirmed the durable toughness of the silica-reinforced OSS against dendritic growth of lithium metal developed during repeated plating/stripping cycles. On the contrary, F was distributed throughout the entire body of plated lithium metal in the nanobead-absent electrolyte

(middle of **Figure 11a**) and the alumina-present electrolyte (middle of **Figure 11c**). The F signals in the lithium metal deposit body possibly originate from the OSS fragments generated after the OSS is broken by protruding dendrites. Unlike the silica nanobeads, the alumina nanobeads did not form robust OSS, which was also evidenced by aluminum signal spread on the entire lithium metal deposit (bottom of **Figure 11c**).

Morphological differences of lithium metal deposits between the absence and the presence of nanobeads were clear after the first metal plating in the $LiPF_6$-based carbonate electrolyte. Typical dendrites of several tens of nm in their thickness at high aspect ratio were observed in the absence of nanobeads (**Figure 12a**). The dendrites grown in the presence of alumina nanobeads were thicker in diameter at larger than 100 nm so that they appeared to be straight columns without tortuous growth shown in the typical dendritic morphologies (**Figure 12g**). The most agglomerated and the least dendritic metal deposit was obtained in the presence of the silica nanobeads (**Figure 12d**). The silica nanobead layer was found above the integrated deposit in the same electron-microscopic image, which was contrasted to the alumina case where there was no alumina layer clearly identified. After the lithium metal plating following 20 plating/stripping cycles, on the other hand, the cross-sectional morphology differences of lithium metal deposits between the absence and the presence of nanobeads became less clear. All lithium metal deposits showed the similar morphologies independent of the existence and kinds of nanobeads, having a more tortuous and thinner dendrites of diameters less than 10 nm than the deposits in the absence of nanobeads after the first metal plating (**Figure 12b**, **e** and **h**).

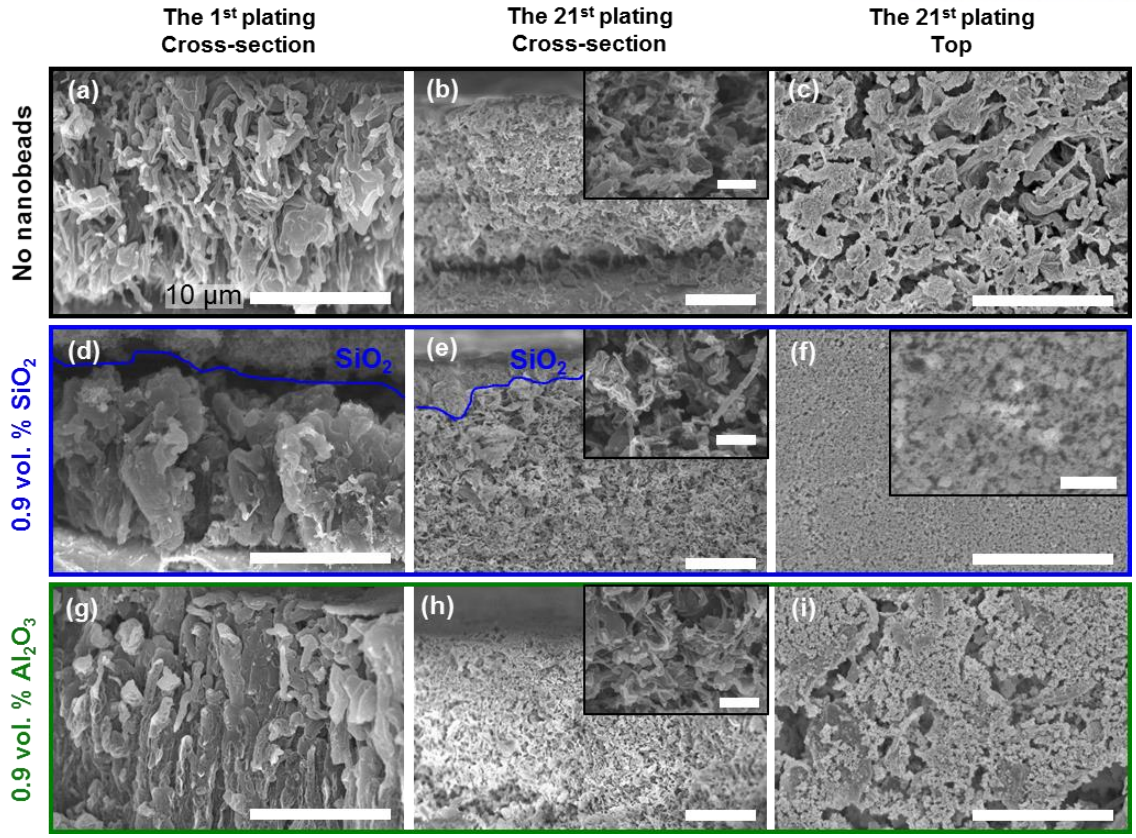

Figure 12. Morphology of lithium metal deposits plated on copper substrates. The electrolyte and the cycling condition were the same as those of **Figure 10**. (**a** to **i**) SEM images of the electrodes in the presence of: (**a** to **c**) no nanobeads, (**d** to **f**) 0.9 vol. % silica and (**g** to **i**) 0.9 vol. % alumina. The left images are for the cross-sectional views of lithium metal deposits obtained after the first plating. The middle and right images are for the cross-sectional and top views of lithium metal deposits obtained after the 20th plating following 19 plating/stripping cycles. 10 μm scale bars were indicated while the scale bar in the inset is 1 μm.

However, the feature size of dendrites (several tens of nm in diameter) observed on the outmost surface did not significantly change in the nanobead-absent case from the first plating to the 21st plating (**Figure 12c**). Also, the heads of columns in over 100 nm shown in the first plating (**Figure 12g**) were peeked through alumina-uncovered surface in the 21st plating (**Figure 12f**). The surface of metal deposit was completely covered by the silica nanobeads even after the twenty times repeated plating/stripping (**Figure 12i**).

Nanobeads were clearly found spread on the surfaces of lithium metal deposits in the top views (**Figure 12f** and **i** for silica and alumina, respectively). Silica nanobeads were more closely packed on the surface than alumina nanobeads even if the same volumetric amount of 0.9 vol. % (nanobead/electrolyte) was used for both nanobeads. The number of particles was also the same since

the particle sizes of silica and alumina nanobeads were similar at ~13 nm. As shown in the elemental maps along the cross-section of lithium deposits (bottoms of **Figure 11b** and **c**), the silica nanobeads were concentrated on the surface but the alumina nanoparticles were dispersed throughout the deposit. The nanobead-reinforced OSS, which prevents the penetration of lithium metal dendrites, was responsible for the increase in cycle life (**Figure 10**). The more surface-confined and more packed silica layers on OSS was more effective than the less packed and more distributed alumina layers in terms of cycle life prolongation (**Figure 12**).

The distinguished difference between silica and alumina is the nanobead density of the outmost surface of OSS (**Figure 12**) determining the OSS toughness (**Figure 11**). A trace amount of HF catalyzes the siloxane bond formation reaction between silane groups:

-Si-OH + HO-Si- → -Si-O-Si- + H_2O.[30]

Fluoride ion (F^-) is coordinated to the silicon atom of –Si-OH or displaces –OH of –Si-OH, making the silicon atom more susceptible to nucleophilic attack by another HO-Si-.[31] Therefore, the interconnected silica nanobead network formation in OSS is possibly expected in $LiPF_6$-based carbonate electrolytes because HF is generated by the reaction between PF_6^- and moisture adsorbed on silica:

$LiPF_6 + H_2O \rightarrow LiF + POF_3 + 2HF$

The integrity of silica nanobead layer is possibly guaranteed by the siloxane bonds between nanobeads. However, alumina nanobeads do not form the interconnected network due to difficulty in forming–Al-O-Al- bonds at the cell condition so that the alumina-containing OSS is mechanically weaker than the silica-containing OSS.[30]

3.3. Chemical compositions of SEI layers

In addition to the mechanical reinforcement by nanobeads, interestingly, the chemical composition of SEI layers changed in the presence of the oxide nanobeads. The relative proportions of LiF / $Li_xP_yOF_z$ on the outmost surface were evaluated similarly regardless of the presence of nanobeads by X-ray photoelectron spectroscopy (XPS) (**Figure 14a**). After etching the surface with argon ion sputtering for 500 s, however, LiF was dominant over $Li_xP_yOF_z$ in the presence of nanobeads when compared with the case where no nanobeads were present **(Fig. 13)**.

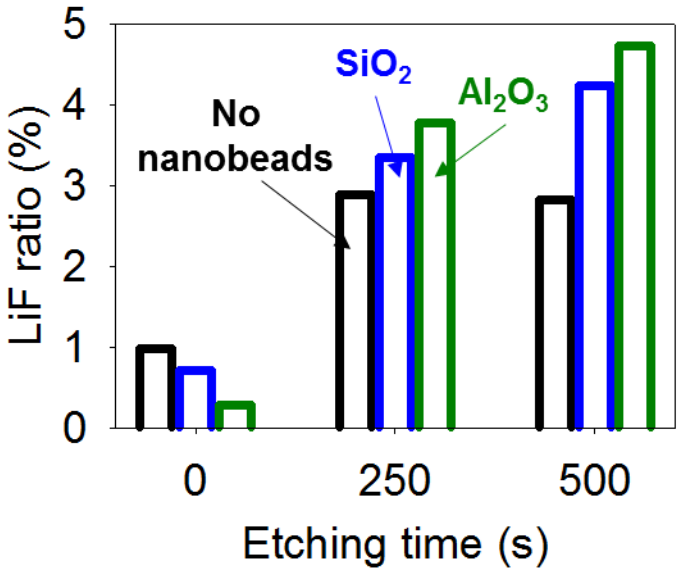

Figure 13. LiF ratio in the SEI layers of each lithium deposit with and without oxide nanobeads. Ratio was calculated from the peak area of each $Li_xP_yOF_z$ and LiF in XPS data of **figure 14**.

The LiF-rich SEI layers were reported to be beneficial in terms of suppressing dendrite growth [25, 32]. In addition, the presence of nanobeads produced SEI layers of high F atom composition (**Figure 14b**). The difference of F atom contents between nanobead-present and nanobead-absent cases were maximized at the surface where $Li_xP_yOF_z$ predominated over LiF. Then, the F composition decreased with depth in nanobead-containing electrolytes. Formation of the F-rich SEI is considered to be due to a trace amount of water absorbed on oxide nanobeads. HF generated from the reaction of water with $LiPF_6$ [33] produces LiF-rich SEI layers providing more facile lithium ion diffusion by:

$LiPF_6 + H_2O \rightarrow LiF + POF_3 + 2HF$; $2HF + 2Li+ + 2e^- \rightarrow 2LiF + H_2$.[32]

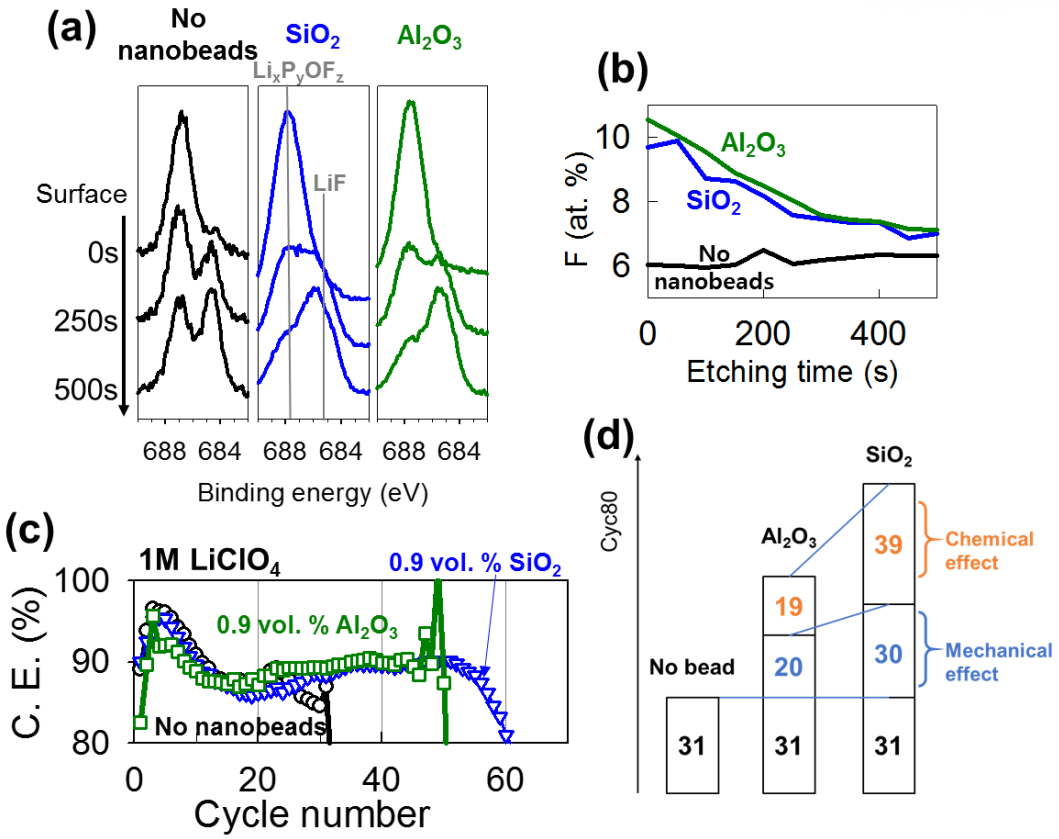

Figure 14. Chemical compositions of OSS. The cycling condition was the same as that of **Figure 10**. 1 wt. % nanobeads were used, which were equivalent to 0.5 vol. % silica and 0.3 vol. % alumina. The $LiPF_6$-based electrolyte of **Figure 10** was used for XPS measurement (**a** and **b**) while the lithium salt was changed to $LiClO_4$ at the same concentration for **c**. (**a**) F 1s XPS spectra. (**b**) The change of the atomic ratio occupied by F with etching time. The F atomic ratio was calculated in consideration of the peak area and relative intensity factor. (**c**) The coulombic efficiency of Li||Cu cells along cycles in the presence of 1 M $LiClO_4$. (**d**) Contribution analysis of mechanical and chemical factors. The effects of the factors were quantified by comparing the cycle life (Cyc80) between the absence and the presence of nanobead in $LiClO_4$ and between the absence and the presence of PF_6^- with nanobeads. Cyc80 was defined as the cycle number at which the coulombic efficiency falls below 80 %.

Benefits of the LiF-rich SEI layers (facile lithium ion transport) were confirmed by the resistance involved in lithium plating/stripping processes. Impedance spectra of Li||Li symmetric cells were measured at open circuit potential around 0 V_{Li} on 3 hours and 3 days after cell assembly without any potential stimulation (**Figure 15**). Potential was not applied to form the SEI layer on lithium metal. Nonetheless, the SEI layer (OSS) is expected to be formed on lithium metals by electrolyte decomposition triggered by the reduction potential of Li^+/Li during the storage period. The charger transfer resistance R_{ct}, including Li^+/Li electrochemistry and lithium transport through the OSS, was

obtained from the diameter of the semi-circles of impedance spectra. Cells containing oxide nanobeads showed lower R_{ct} than the nanobead-absent control cell over all oxide contents in both 3 hours and 3 days measurements. The R_{ct} increased along time as the OSS formation was evolved. In the measurement on 3 hours, both silica and alumina nanobeads exhibited the similar values of R_{ct}. The R_{ct} decreased with oxide contents. However, alumina became superior to silica especially at oxide contents higher than 0.3 wt. % in terms of R_{ct} in the 3 days measurement. The R_{ct} of alumina decreased with oxide contents while the R_{ct} of silica did not change. The oxide content dependency of R_{ct} on both 3 hours and 3 days is easily understood since HF generated by the moisture adsorbed on alumina is totally used for forming LiF-rich SEI layer. The amount of alumina is directly related to the LiF contents in SEI layer and higher LiF-rich composition of OSS encourages lower R_{ct}.

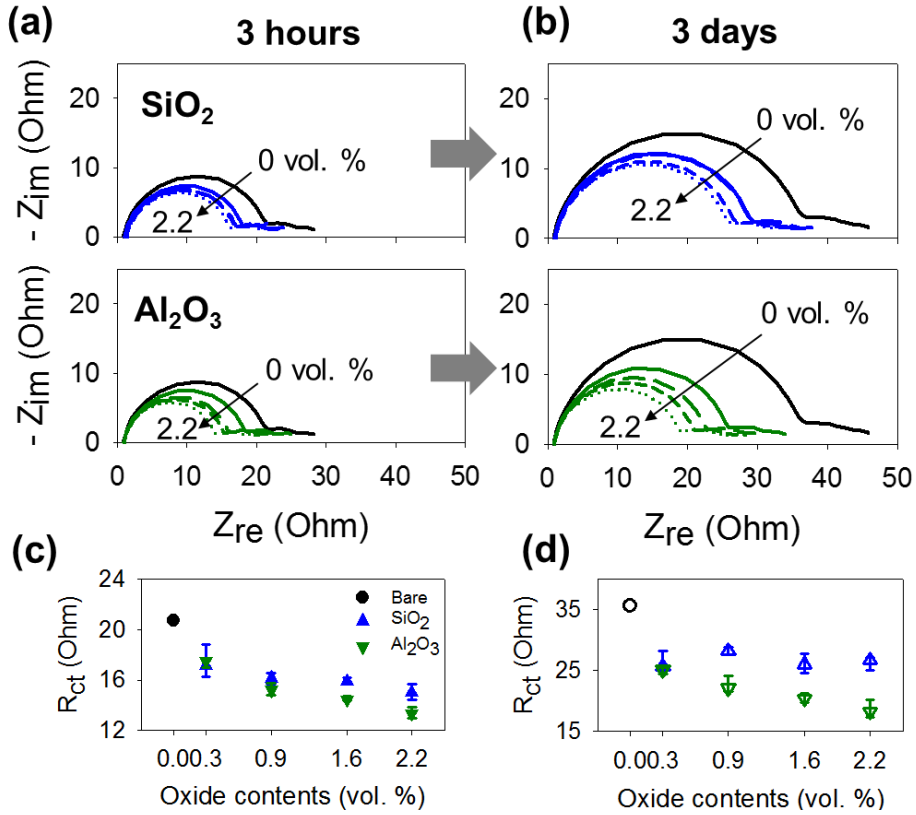

Figure 15. Charge transfer resistances (R_{ct}) of Li^+/Li^0 electrochemistry on 3 hours and 3 days after cell assembly. (**a** and **b**) Impedance spectra of Li||Li cells. Potential was biased at the open circuit potential around 0 V_{Li}. The $LiPF_6$-based electrolyte of **Figure 10** was used. (**c** and **d**) Nanobead content dependency of R_{ct}. Averages and standard deviations were calculated from three different independent tests. Impedances were measured on 3 hours (**a** and **c**) and 3 days (**b** and **d**) after the cell assembly.

In the presence of silica, on the contrary, the HF generated by the moisture adsorbed on silica is

utilized in two different ways: for interconnecting silica nanobeads via the HF-catalyzed sol-gel reaction as well as forming LiF-rich SEI layer. Even if HF is not consumed by the siloxane bond formation (therefore, HF is considered as a catalyst), it was reported that fluoride is included in HF-catalyzed gel structures.[31] The F^- coordination to silicon could be conserved in a form of weaker coordination even after the siloxane bond formation. The proportional dependency of R_{ct} on oxide content of silica on 3 hours was interpreted in the same way of the alumina case. In this earlier stage, the LiF-rich OSS formation is thought to be dominant over the siloxane bond (-Si-O-Si-) formation. F^- coordination to surface silicon atom of silica nanobeads would be much slower than that of oligomeric siloxane species formed from widely used silicon alkoxide precursors such as tetramethylorthosilicate (TMOS) during sol-gel reactions. When the SEI layer is fully formed with enough duration, however, it appears that the siloxane formation is dominant over the LiF-rich SEI formation. The majority of HF is consumed for making the siloxane bonds without losing its coordination to silicon. Therefore, the silica content insignificantly affects the LiF-rich SEI formation during the latter stage of SEI layer formation.

To eliminate the benefits of LiF-rich OSS compositions induced by nanobeads and therefore to investigate only the mechanical effects of nanobeads on cell performances, Li||Cu cells were Galvano-statically cycled in a $LiPF_6$-absent electrolyte where $LiClO_4$ was used (**Figure 14c**). The absence of $LiPF_6$ eliminates the opportunities of HF and LiF formation while $LiClO_4$-containing electrolytes are not sensitive to moisture [34]. Both nanobeads still improved cyclability of the Li||Cu cells in the $LiClO_4$-containing electrolyte, confirming the mechanical effects of nanobeads. The cycle number at which the coulombic efficiency (C.E.) falls below 80 % (Cyc@80%) was recorded at 32 for the nanobead-absent cell, 51 for the 0.9 vol. % alumina-present cell and 61 for the 0.9 vol. % silica-present cell. It should be notified that the cyclability of the $LiClO_4$-based cells was much worse than that of the $LiPF_6$-based cells. For example, the Cyc@80% of 0.9 vol. % silica decreased from 100 to 61 when $LiPF_6$ was replaced by $LiClO_4$ (**Figure 10a** to **Figure 14c**). The difference of cyclability between the different lithium salts is caused by the effect of LiF-rich SEI compositions induced by nanobeads (chemical effects of nanobeads).

Contributions of the two factors, mechanical and chemical factors of nanobeads, were quantitatively compared by using Cyc@80% as a measure of the effect of each factor (**Figure 14d**). 20 cycles (= alumina - no nanobead in $LiClO_4$) were improved by the mechanical factor of alumina nanobead and then 19 cycle improvement (alumina in $LiPF_6$ - alumina in $LiClO_4$) by its chemical factor followed. Both the mechanical and chemical effects were intensified when silica was used as the nanobead. The denser and surface-confined nanobead layer of silica in OSS is responsible for the 30 cycles improvement by the mechanical factor (c.f., 20 cycles for alumina). The chemical effect of silica was too strong to consider that it has the same origin of the chemical effect of alumina (39 for silica versus

19 for alumina). In addition to the LiF-rich SEI formation by a trace amount of moisture adsorbed on nanobeads, therefore, the HF-catalyzed siloxane bond formation leading to an interconnected silica nanobead network would contribute significantly to the chemical effect of silica. The additionally suggested factor is considered as the chemical factor because it was initiated by HF formation in the presence of PF_6^-. From the viewpoint of effects, however, it could be categorized to the mechanical factor because the resultant interconnected nanobead layer reinforces the OSS.

IV. Conclusion

In this work, we identified the existence and the role of the OSS that is the SEI layers formed on current collectors (or lithium metal) before the first lithium metal deposition. The mechanical toughness of OSS was the determining factor to suppress dendritic growth of lithium metal and prevent the dendrites from penetrating the OSS. Oxide nanobeads dispersed in electrolytes were incorporated in the OSS during the first SEI layer formation, reinforcing the OSS that is intrinsically brittle and fragile. The resultant nanobead-reinforced OSS dramatically improved the reversibility of lithium metal plating and stripping. In addition to the mechanical effect, the moisture adsorbed on oxide nanobeads encouraged the OSS and the SEI layers in lithium metal deposit to be LiF-rich. The LiF-rich SEI layers supported the facile lithium ion transport (chemical effect). The silica-nanobead-reinforced OSS was more robust than the alumina counterpart, keeping its integrity even after long-term cycles of lithium metal plating and stripping. HF-catalyzed siloxane bond formation between silica nanobeads is expected to form an interconnected silica nanobead network in the upmost layer of OSS, strengthening the OSS mechanically.

V. References

1. Whittingham, M. S., Lithium batteries and cathode materials. *Chemical reviews* **2004,** *104* (10), 4271-4302.

2. Xu, K., Electrolytes and interphases in Li-ion batteries and beyond. *Chemical Reviews* **2014,** *114* (23), 11503-11618.

3. Gubbi, J.; Buyya, R.; Marusic, S.; Palaniswami, M., Internet of Things (IoT): A vision, architectural elements, and future directions. *Future Gener Comp Sy* **2013,** *29* (7), 1645-1660.

4. Etacheri, V.; Marom, R.; Elazari, R.; Salitra, G.; Aurbach, D., Challenges in the development of advanced Li-ion batteries: a review. *Energy & Environmental Science* **2011,** *4* (9), 3243-3262.

5. Mizushima, K.; Jones, P. C.; Wiseman, P. J.; Goodenough, J. B., LixCoO2 (0<x<-1): A new cathode material for batteries of high energy density. *Materials Research Bulletin* **1980,** *15* (6), 783-789.

6. Liu, W.; Oh, P.; Liu, X.; Lee, M. J.; Cho, W.; Chae, S.; Kim, Y.; Cho, J., Nickel-rich layered lithium transition-metal oxide for high-energy lithium-ion batteries. *Angew Chem Int Ed Engl* **2015,** *54* (15), 4440-57.

7. Thackeray, M. M.; Kang, S.-H.; Johnson, C. S.; Vaughey, J. T.; Benedek, R.; Hackney, S., Li 2 MnO 3-stabilized LiMO 2 (M= Mn, Ni, Co) electrodes for lithium-ion batteries. *Journal of Materials chemistry* **2007,** *17* (30), 3112-3125.

8. Scrosati, B., Recent advances in lithium ion battery materials. *Electrochimica Acta* **2000,** *45* (15-16), 2461-2466.

9. Yoshio, M.; Wang, H. Y.; Fukuda, K.; Umeno, T.; Dimov, N.; Ogumi, Z., Carbon-coated Si as a lithium-ion battery anode material. *Journal of the Electrochemical Society* **2002,** *149* (12), A1598-A1603.

10. Xu, W.; Wang, J.; Ding, F.; Chen, X.; Nasybulin, E.; Zhang, Y.; Zhang, J. G., Lithium metal anodes for rechargeable batteries. *Energy and Environmental Science* **2014,** *7* (2), 513-537.

11. Xu, C.; Ahmad, Z.; Aryanfar, A.; Viswanathan, V.; Greer, J. R., Enhanced strength and temperature dependence of mechanical properties of Li at small scales and its implications for Li metal anodes. *Proceedings of the National Academy of Sciences of the United States of America* **2017,** *114* (1), 57-61.

12. Aurbach, D.; Zinigrad, E.; Cohen, Y.; Teller, H., A short review of failure mechanisms of lithium metal and lithiated graphite anodes in liquid electrolyte solutions. *Solid State Ionics* **2002,** *148* (3-4), 405-416.

13. Lv, D.; Shao, Y.; Lozano, T.; Bennett, W. D.; Graff, G. L.; Polzin, B.; Zhang, J.; Engelhard, M. H.; Saenz, N. T.; Henderson, W. A.; Bhattacharya, P.; Liu, J.; Xiao, J., Failure mechanism for fast-charged lithium metal batteries with liquid electrolytes. *Advanced Energy Materials* **2015,** *5* (3).

14. Yamaki, J.-i.; Tobishima, S.-i.; Hayashi, K.; Keiichi, S.; Nemoto, Y.; Arakawa, M., A consideration of the morphology of electrochemically deposited lithium in an organic electrolyte. *Journal of Power Sources* **1998,** *74* (2), 219-227.

15. Wang, D.; Zhang, W.; Zheng, W.; Cui, X.; Rojo, T.; Zhang, Q., Towards High-Safe Lithium Metal Anodes: Suppressing Lithium Dendrites via Tuning Surface Energy. *Advanced Science* **2017,** *4* (1).

16. Peng, Z.; Wang, S.; Zhou, J.; Jin, Y.; Liu, Y.; Qin, Y.; Shen, C.; Han, W.; Wang, D., Volumetric variation confinement: Surface protective structure for high cyclic stability of lithium metal electrodes. *Journal of Materials Chemistry A* **2016,** *4* (7), 2427-2432.

17. Zhu, B.; Jin, Y.; Hu, X.; Zheng, Q.; Zhang, S.; Wang, Q.; Zhu, J., Poly(dimethylsiloxane) Thin Film as a Stable Interfacial Layer for High-Performance Lithium-Metal Battery Anodes. *Adv Mater* **2017,** *29* (2).

18. Lang, J.; Song, J.; Qi, L.; Luo, Y.; Luo, X.; Wu, H., Uniform Lithium Deposition Induced by Polyacrylonitrile Submicron Fiber Array for Stable Lithium Metal Anode. *ACS Applied Materials and Interfaces* **2017,** *9* (12), 10360-10365.

19. Lu, Y. Y.; Tikekar, M.; Mohanty, R.; Hendrickson, K.; Ma, L.; Archer, L. A., Stable Cycling of Lithium Metal Batteries Using High Transference Number Electrolytes. *Advanced Energy Materials* **2015,** *5* (9).

20. Suo, L.; Hu, Y. S.; Li, H.; Armand, M.; Chen, L., A new class of Solvent-in-Salt electrolyte for high-energy rechargeable metallic lithium batteries. *Nature Communications* **2013,** *4*.

21. Byrne, N.; Howlett, P. C.; MacFarlane, D. R.; Forsyth, M., The zwitterion effect in ionic liquids: Towards practical rechargeable lithium-metal batteries. *Advanced Materials* **2005,** *17* (20), 2497-2501.

22. Park, J.; Jeong, J.; Lee, Y.; Oh, M.; Ryou, M. H.; Lee, Y. M., Micro-Patterned Lithium Metal Anodes with Suppressed Dendrite Formation for Post Lithium-Ion Batteries. *Advanced Materials Interfaces* **2016,** *3* (11).

23. Zhang, R.; Cheng, X. B.; Zhao, C. Z.; Peng, H. J.; Shi, J. L.; Huang, J. Q.; Wang, J.; Wei, F.; Zhang, Q., Conductive Nanostructured Scaffolds Render Low Local Current Density to Inhibit Lithium Dendrite Growth. *Advanced Materials* **2016,** *28* (11), 2155-2162.

24. Li, W.; Yao, H.; Yan, K.; Zheng, G.; Liang, Z.; Chiang, Y. M.; Cui, Y., The synergetic effect of lithium polysulfide and lithium nitrate to prevent lithium dendrite growth. *Nat Commun* **2015,** *6*, 7436.

25. Zhang, X. Q.; Cheng, X. B.; Chen, X.; Yan, C.; Zhang, Q., Fluoroethylene Carbonate Additives to Render Uniform Li Deposits in Lithium Metal Batteries. *Advanced Functional Materials* **2017,** *27* (10).

26. Zheng, J.; Engelhard, M. H.; Mei, D.; Jiao, S.; Polzin, B. J.; Zhang, J.-G.; Xu, W., Electrolyte additive enabled fast charging and stable cycling lithium metal batteries. *Nature Energy* **2017,** *2*, 17012.

27. Kozen, A. C.; Lin, C. F.; Pearse, A. J.; Schroeder, M. A.; Han, X.; Hu, L.; Lee, S. B.; Rubloff, G. W.; Noked, M., Next-Generation Lithium Metal Anode Engineering via Atomic Layer Deposition. *ACS Nano* **2015,** *9* (6), 5884-5892.

28. Kim, J. H.; Woo, H. S.; Kim, W. K.; Ryu, K. H.; Kim, D. W., Improved Cycling Performance of Lithium-Oxygen Cells by Use of a Lithium Electrode Protected with Conductive Polymer and Aluminum Fluoride. *ACS Applied Materials and Interfaces* **2016,** *8* (47), 32300-32306.

29. Li, N. W.; Yin, Y. X.; Yang, C. P.; Guo, Y. G., An Artificial Solid Electrolyte Interphase Layer for Stable Lithium Metal Anodes. *Advanced Materials* **2016,** *28* (9), 1853-1858.

30. Brinker, C. J.; Scherer, G. W., *Sol-gel science: the physics and chemistry of sol-gel processing*. Academic press: 2013.

31. Winter, R.; Chan, J. B.; Frattini, R.; Jonas, J., The Effect of Fluoride on the Sol-Gel Process. *Journal of Non-Crystalline Solids* **1988,** *105* (3), 214-222.

32. Qian, J.; Xu, W.; Bhattacharya, P.; Engelhard, M.; Henderson, W. A.; Zhang, Y.; Zhang, J.-G., Dendrite-free Li deposition using trace-amounts of water as an electrolyte additive. *Nano Energy* **2015,** *15*, 135-144.

33. Plakhotnyk, A. V.; Ernst, L.; Schmutzler, R., Hydrolysis in the system LiPF6—propylene carbonate—dimethyl carbonate—H2O. *Journal of Fluorine Chemistry* **2005,** *126* (1), 27-31.

34. Younesi, R.; Veith, G. M.; Johansson, P.; Edström, K.; Vegge, T., Lithium salts for advanced lithium batteries: Li–metal, Li–O2, and Li–S. *Energy & Environmental Science* **2015,** *8* (7), 1905-1922.